atmosphere

MDPI

Article

Evaluating a WRF Multi-Physics Ensemble for Historical Climate Simulations over the CORDEX-EA Phase 2 Domain

Tae-Jun Kim [1], Jin-Uk Kim [1,*], Jae-Kwan Shim [1], Myung-Ju Choi [1], Kyung-On Boo [1], Seung-Ki Min [2], Dong-Hyun Cha [3] and Eun-Chul Chang [4]

[1] Climate Change Research Team, National Institute of Meteorological Sciences, Seogwipo 63568, Republic of Korea
[2] Division of Environmental Science and Engineering, Pohang University of Science and Technology, Pohang 37673, Republic of Korea
[3] Department of Civil, Urban, Earth, and Environmental Engineering, Ulsan National Institute of Science and Technology, Ulsan 44919, Republic of Korea
[4] Department of Atmospheric Science, Kongju National University, Gongju 32588, Republic of Korea
* Correspondence: jukim86@korea.kr

Abstract

In this study, we comprehensively evaluate the simulation performance of a 12 km high-resolution multi-physics ensemble of the Weather Research and Forecasting (WRF) model, utilizing the CORDEX-East Asia (CORDEX-EA) Phase 2 grid domain. An eight-member ensemble was constructed by combining two schemes each for microphysics (MPS), planetary boundary layer (PBL), and cumulus parameterization (CPS). Although continuous simulations were conducted for a 46-year period (1979–2024), this performance evaluation focuses on various variables during a recent 20-year period (2005–2024). Validated against observational and reanalysis datasets, the ensemble members demonstrated highly capable overall performance for the surface and low tropospheric variables, with Taylor skill scores exceeding 0.7. However, simulation performance varied substantially across variables, seasons, and physics scheme combinations, with mean bias remaining a crucial factor to be considered. They successfully captured the spatiotemporal patterns of temperature and precipitation, albeit with distinct sensitivities to the chosen physics combinations. In particular, the CPS–PBL combination played the critical role in shaping inter-model variabilities through modulating precipitation over the Western North Pacific. The ensemble mean approach mitigated the sensitivities associated with individual physics configurations, thereby demonstrating robust overall performance. Further analysis for the Korean Peninsula reveals that the influence of physics combinations depends on the target analysis region. These results offer critical scientific insights into optimal physics selection and ensemble configuration for climate change scenarios over East Asia, while also providing a solid foundation for interpreting future regional climate projections based on the upcoming AR7 scenarios.

Keywords: CORDEX-EA; WRF; evaluation; multi-physics

Academic Editor: Stefan Grab

Received: 29 September 2026
Revised: 30 October 2026
Accepted: 10 November 2026
Published: 12 November 2026

Copyright: © 2026 by the authors. Licensee MDPI, Basel, Switzerland. This article is an open access article distributed under the terms and conditions of the Creative Commons Attribution (CC BY) license.

1. Introduction

The Sixth Assessment Report (AR6) of the Intergovernmental Panel on Climate Change (IPCC) states that anthropogenic greenhouse gas emissions have driven global climate change, significantly increasing the frequency and intensity of extreme weather events such as droughts, heatwaves, heavy precipitation, and typhoons. Furthermore, climate change poses a severe threat not only to human socio-economic sectors—including food security, water resources, and public health—but also to entire ecosystems, with these impacts projected to intensify in the future [1].

In climate change research, Global Climate Models (GCMs) are primarily used as tools to understand the global climate system and predict future changes. However, due to enormous computational demands, GCMs are typically run at horizontal resolutions ranging from tens to hundreds of kilometers. Consequently, they are limited in their ability to reproduce mesoscale convective systems that develop at sub-grid scales, as well as localized atmospheric phenomena in regions with complex topography and coastlines [2–4].

To overcome these limitations of GCMs, dynamical downscaling techniques utilizing Regional Climate Models (RCMs) are widely employed. By utilizing GCM outputs as boundary conditions, RCMs have the advantage of preserving the synoptic-scale climate system information provided by GCMs while detailing regional climate features through high-resolution grid systems and sophisticated physical parameterizations [5–7]. However, RCM simulations exhibit variability and uncertainty depending on the model structure and the chosen combinations of physical parameterizations. Therefore, continuous efforts have been made to employ multi-model or multi-physics ensembles to improve simulation reliability and evaluate these uncertainties [8–10]. While early RCM studies were conducted under individual domains and conditions, making intercomparisons difficult, the launch of the Coordinated Regional Climate Downscaling Experiment (CORDEX) under the World Climate Research Programme (WCRP) has facilitated active collaborative research to compare and validate diverse RCM results within an internationally standardized framework [11,12]. Recently, next-generation climate change scenarios have been released in preparation for the IPCC Seventh Assessment Report (AR7) [13]. With the rapidly growing demand across various sectors for regional climate projection data, the need for high-resolution regional climate projections based on these new scenarios has also increasingly emerged within the CORDEX community [14,15].

In South Korea, researchers from the National Institute of Meteorological Sciences (NIMS) and academia have participated in the CORDEX-East Asia (CORDEX-EA) group, producing 25 km horizontal resolution climate change projections for East Asia based on the IPCC Fifth Assessment Report (AR5) and AR6 scenarios [16–18]. These datasets have been provided to climate researchers both within South Korea and globally, significantly contributing to the advancement of climate change research. They have also been utilized as forcing data for the detailed climate change scenarios for South Korea by the Korea Meteorological Administration (KMA), thereby providing a scientific foundation for establishing national climate crisis response policies and impact assessments. The South Korean CORDEX-EA experiments based on the AR5 and AR6 scenarios constructed an ensemble system using five different RCMs. However, multi-model ensembles have a limitation: if a specific RCM possesses large systematic biases, it can heavily influence the overall ensemble results. Considering this drawback, the recent CORDEX-CORE project—which promotes downscaling based on globally standardized RCM experimental setups—has configured climate data downscaling using only a limited number of RCMs selected for their simulation capabilities and performance. Similarly, the South Korean CORDEX-EA research group is currently striving to diversify its ensemble configurations

https://doi.org/10.3390/atmos17111118

[15,19]. The Weather Research and Forecasting (WRF) model is one of the representative RCMs operated by South Korean research teams participating in CORDEX-EA and is also an RCM member used in CORDEX-CORE. Developed primarily by the National Center for Atmospheric Research (NCAR), it is now widely utilized in operational weather forecasting and climate research [20]. Furthermore, it supports various parameterization schemes in a modular format for diverse sub-grid scale physical processes—such as cloud microphysics, cumulus convection, planetary boundary layer, and radiation—providing the advantage of configuring optimal physics combinations tailored to the characteristics of the target region [21,22]. Particularly in regional climate simulations with horizontal resolutions around 10 km, the selection of physical parameterizations significantly impacts simulation errors and performance. Therefore, the WRF model's ability to utilize diverse parameterization schemes makes its strengths highly prominent in this context [23–25].

Accordingly, this study aims to conduct a 12 km high-resolution multi-physics ensemble evaluation experiment using the WRF model over the CORDEX-EA Phase 2 domain. By validating the simulation performance of 20 variables—including temperature, precipitation, lower-level atmospheric circulation, radiation, and pressure—across the eight-member multi-physics ensemble experiments, and by comparing the characteristics of each ensemble member for key variables, this study seeks to establish a solid scientific foundation for analyzing and utilizing future regional climate projections based on the new AR7 scenarios.

2. Materials and Methods

Simulations in this study were conducted using the nonhydrostatic Weather Research and Forecasting (WRF) model version 4.4 [20], developed by the National Center for Atmospheric Research (NCAR). Detailed model configurations are summarized in Table 1, Figures 1 and 2. The simulation domain was configured based on the CORDEX-EA Phase 2 framework at a 12 km horizontal resolution (Figure 1), which encompasses the East Asian continent, India, and parts of the Western Pacific, making it well-suited for investigating the East Asian monsoon and tropical cyclones. However, the primary evaluation domain for model performance in this study is bounded by a solid red line in Figure 1 (EA: 80–150° E, 10–55° N), whereas the analysis results for the Korean Peninsula, bounded by a dashed red line (KOR: 124–131° E, 33–43° N), are provided in the Supplementary Materials. Along the vertical axis, a hybrid vertical coordinate system comprising 35 layers from the surface to 50 hPa was employed, with an integration time step of 36 s. The Unified Noah scheme [26] and the Rapid Radiative Transfer Model for GCMs (RRTMG) scheme [27] were selected for land surface and radiation processes, respectively. Initial and lateral boundary conditions were provided by the fifth-generation European Center for Medium-Range Weather Forecasts (ECMWF) reanalysis (ERA5) dataset [28] at 6 h intervals. Spectral nudging was applied, and a buffer zone of 20 grid cells was established along each lateral boundary. The overall simulation period spans 46 years (1979–2024); referencing the historical evaluation criteria provided by KMA, the recent 20-year period from 2005 to 2024 was designated as the primary analysis period.

Table 1. Model configurations used in this study.

Contents	Description
Horizontal resolution	Lon. × Lat.: 825 × 521 (12 km)
Map projection	Lambert Conformal
Reference position	116.57° E, 34.40° N (True Lat.1: 20° N, Lat.2: 40° N)

Vertical layer (top)	35 hybrid sigma-pressure levels (50 hPa)
Land surface model	Unified Noah
Long/Short wave radiation scheme	RRTMG
Time step	36 s
Spectral nudging	Yes
Buffer zone	20 grid points
Reference data	CPC(0.5° × 0.5°): tas/tasmax/tasmin IMERG(0.1° × 0.1°): pr ERA5(0.25° × 0.25°): others
Analysis region	EA: 80~150° E, 10~55° N KOR: 124~131° E, 33~43° N

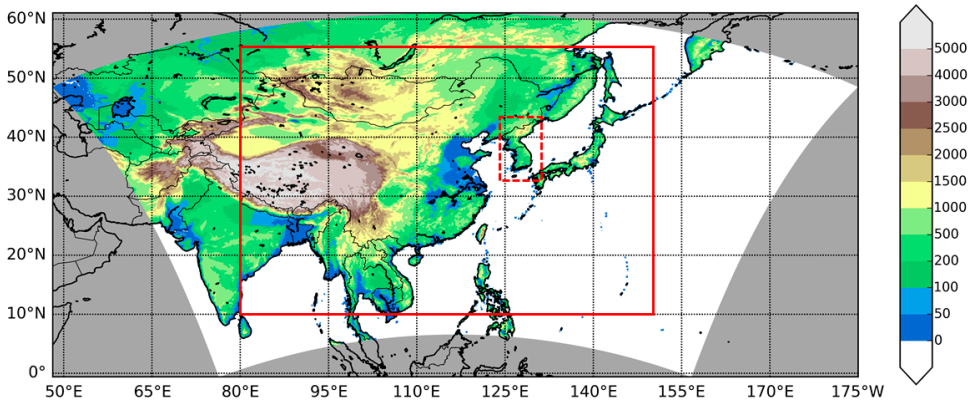


Figure 1. Model domain and topography (m) used in this study. The solid red line indicates the East Asia (EA) analysis region, and the red dotted line denotes the Korean Peninsula (KOR) region.

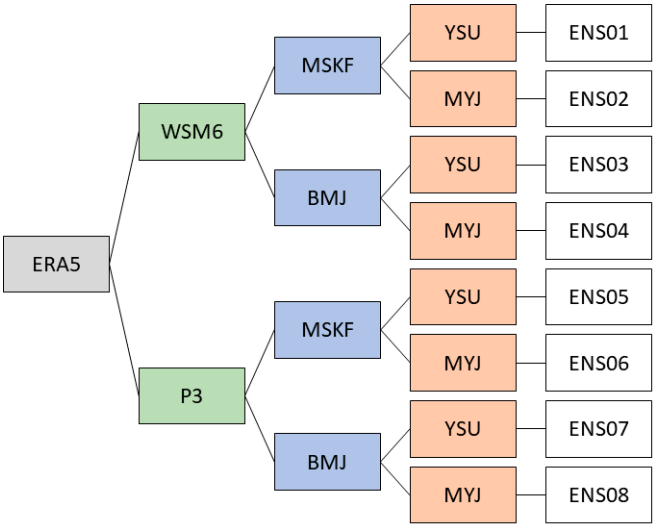


Figure 2. Configuration of the physical parameterization ensemble used in this study. Eight ensemble members (ENS01–ENS08) were generated by combining two microphysics schemes (WSM6 and P3), two cumulus parameterization schemes (MSKF and BMJ), and two planetary boundary layer schemes (YSU and MYJ).

The configuration of the multi-physics ensemble combinations is illustrated in Figure 2. Two schemes with distinct physical characteristics were selected for each of three key physical processes: the microphysics scheme (MPS), cumulus parameterization scheme (CPS), and planetary boundary layer scheme (PBL). Combining these schemes resulted in

eight multi-physics ensemble members (ENS01–ENS08). For the MPS, we selected the WRF Single-Moment 6-class microphysics scheme (WSM6) [29]—which distinguishes six water species (water vapor, cloud water, rain, ice, snow, and graupel) to simulate microphysical phase changes—and the Predicted Particle Properties (P3) scheme [30], which predicts the mass and volume of ice particles to represent variations in particle size and density. For the CPS, the Multi-Scale Kain–Fritsch (MSKF) [31] and Betts–Miller–Janjić (BMJ) [32] schemes were adopted; MSKF accounts for convective transport by updrafts and downdrafts via a mass-flux approach, whereas BMJ simulates sub-grid scale convection using a convective adjustment approach that relaxes the atmospheric thermodynamic state toward post-convective reference vertical profiles. For PBL physics, the Yonsei University (YSU) [33] and Mellor–Yamada–Janjić (MYJ) [32] schemes were chosen; YSU incorporates non-local transport driven by large eddies alongside local mixing, whereas MYJ simulates local turbulent mixing based on Turbulent Kinetic Energy (TKE).

The target variables analyzed in this study are listed in Table 2. Comprehensive quantitative evaluations using Taylor diagrams and Taylor skill scores (TSS) [34] were conducted for all variables. Additionally, an analysis of variance (ANOVA)-based contribution analysis [35] was performed to quantify the relative influence of individual physics scheme choices and their interactions on the total ensemble spread. For each atmospheric variable and ensemble member, climatological seasonal mean values averaged over the analysis period were utilized as input data. Using a three-way ANOVA framework, the sums of squares were calculated for the main effects of the three physical parameterizations, two-way interactions, and the three-way interaction. The relative contribution of each component was then quantified as the ratio of its sum of squares to the total sum of squares. Furthermore, spatial distributions and time-series evaluations are presented for temperature and precipitation, which are key target variables in regional climate performance evaluations. Because ERA5 reanalysis data were used for initial and boundary conditions, model validation for temperature and precipitation was objectively conducted using independent observation-based datasets, specifically Climate Prediction Center (CPC) [36] and Integrated Multi-satellitE Retrievals for GPM (IMERG) [37]. For the remaining atmospheric variables, due to the limited availability of continuous gridded observational datasets over East Asia, model fidelity was evaluated against the ERA5 reanalysis dataset. Hereafter, these reference observational and reanalysis datasets are collectively referred to as OBS for brevity and consistency.

Table 2. Summary of surface and atmospheric variables evaluated in this study.

Variables	Description	Units	Level
tas	Near-surface air temperature	°C	Surface
tasmax	Daily maximum near-surface air temperature	°C	
tasmin	Daily minimum near-surface air temperature	°C	
ts	Surface temperature	°C	
rsds	Surface downwelling shortwave radiation	W m^{-2}	
rlds	Surface downwelling longwave radiation	W m^{-2}	
hfls	Surface upward latent heat flux	W m^{-2}	
hfss	Surface upward sensible heat flux	W m^{-2}	
ps	Surface air pressure	hPa	
psl	Sea level pressure	hPa	
pr	Precipitation	mm day^{-1}	
evspsbl	Evaporation including sublimation and transpiration	kg m^{-2} s^{-1}	
uas	Eastward near-surface wind	m s^{-1}	
vas	Northward near-surface wind	m s^{-1}	

sfcWindmax	Daily maximum near-surface wind speed	m s^{-1}	
sfcWind	Near-surface wind speed	m s^{-1}	
ua850	Eastward wind at 850 hPa	m s^{-1}	Upper-air
va850	Northward wind at 850 hPa	m s^{-1}	
ta850	Air temperature at 850 hPa	°C	
hus850	Specific humidity at 850 hPa	kg kg^{-1}	

3. Results

Figure 3 presents Taylor diagrams to evaluate the seasonal spatial pattern performance of 20 variables across the ensemble members and the ensemble mean (EM). Although the simulation performance of the ensemble members was generally high, lower performance was observed for certain variables, such as hfss and vas, demonstrating noticeable inter-variable variations (Figure 3a). For most variables, inter-member differences were minimal; however, pr exhibited a relatively wide range of normalized standard deviations, which was primarily driven by substantial variations in simulation performance among ensemble members during summer (Figure 3d) and autumn (Figure 3e). Seasonally, winter showed the highest correlation coefficients, with normalized standard deviations for most variables falling between 0.5 and 1.5, representing the overall best performance. Spring performance was also generally reliable, although low correlations for vas were consistently observed across all ensemble members. In summer, correlations for precipitation were relatively low, and ENS03 and ENS07 displayed large normalized standard deviations for hfls and evspsbl. In autumn, simulation skill for hfss, uas, vas, and va850 tended to be lower overall; nevertheless, the differences among ensemble members were small, suggesting that these features reflect systematic model characteristics. The EM effectively mitigated the sensitivities of individual members, demonstrating robust overall performance in both spatial correlation coefficients and normalized standard deviations. While Taylor diagrams are useful for evaluating spatial pattern similarity, they have limitations in capturing mean value biases. Therefore, quantitative evaluation results—including OBS means, EM biases and RMSEs, and the range of member biases and RMSEs—are provided in Table 3 (winter and summer) and discussed below.

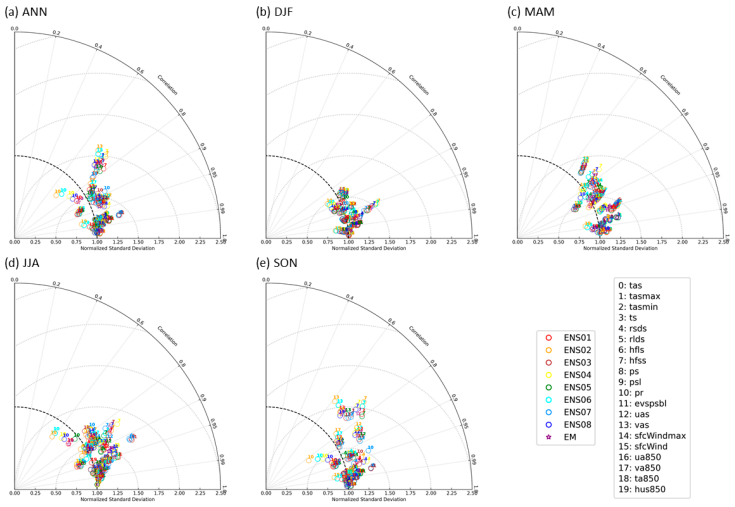


Figure 3. Taylor diagrams showing the performance of individual ensemble members (ENS01-ENS08) and the EM relative to OBS for (**a**) annual (ANN), (**b**) DJF, (**c**) MAM, (**d**) JJA, and (**e**) SON using normalized standard deviation and spatial correlation. The color and number assigned to each point are indicated in the legend.

Table 3. DJF and JJA statistics for each variable over the East Asia: observation (OBS) mean, ensemble mean (EM) bias and RMSE. Values in parentheses indicate the minimum–maximum range among ensemble members.

Season	Variables	OBS Mean	Bias	RMSE
DJF	tas	−4.57	−1.13 (−1.28~−0.94)	3.45 (3.37~3.58)
	tasmax	1.16	−1.36 (−1.47~−1.20)	3.58 (3.51~3.65)
	tasmin	−10.30	−0.49 (−0.67~−0.25)	3.66 (3.55~3.88)
	ts	4.60	0.01 (−0.17~0.21)	2.15 (2.08~2.30)
	rsds	133.95	19.75 (11.33~26.63)	23.66 (18.59~30.83)
	rlds	280.12	−5.92 (−10.07~−1.78)	9.24 (7.58~12.60)
	hfls	85.49	5.74 (1.68~9.21)	16.09 (13.94~20.62)
	hfss	26.19	5.34 (4.04~6.91)	14.65 (12.25~17.74)
	ps	939.71	1.38 (1.16~1.61)	7.60 (7.55~7.67)
	psl	1020.10	2.09 (1.62~2.56)	2.67 (2.18~3.23)
	pr	1.42	0.11 (−0.03~0.23)	0.76 (0.77~0.92)
	evspsbl	0.000034	0.000002 (0.000001~0.000004)	0.000006 (0.000005~0.000008)
	uas	−0.33	0.21 (0.16~0.27)	1.31 (1.30~1.33)
	vas	−1.73	0.00 (−0.02~0.01)	1.16 (1.12~1.22)
	sfcWindmax	7.93	0.21 (0.15~ 0.30)	1.01 (1.01~1.04)
	sfcWind	4.80	1.00 (0.95~1.04)	1.45 (1.43~1.47)
	ua850	1.29	0.13 (0.09~0.19)	0.80 (0.76~0.86)
	va850	−1.54	0.04 (−0.01~0.07)	1.15 (1.11~1.19)
	ta850	1.59	−0.38 (−0.47~−0.33)	0.61 (0.58~0.68)
	hus850	0.004601	−0.000289 (−0.000544~−0.000062)	0.000527 (0.000329~0.000862)
JJA	tas	20.67	−0.44 (−0.67~−0.18)	2.26 (2.22~2.34)
	tasmax	26.01	−0.78 (−1.13~−0.50)	2.54 (2.45~2.77)
	tasmin	15.32	−0.09 (−0.37~0.20)	2.18 (2.17~2.27)
	ts	22.94	0.71 (0.27~1.23)	1.49 (1.23~2.12)
	rsds	228.57	42.13 (26.68~54.47)	45.13 (33.02~57.27)
	rlds	381.04	−3.09 (−5.59~−0.18)	7.10 (6.76~8.56)
	hfls	83.40	4.87 (−5.40~15.25)	18.83 (17.35~31.54)
	hfss	23.13	10.26 (5.12~14.96)	17.65 (14.15~22.35)
	ps	932.22	0.11 (−0.85~1.05)	6.81 (6.81~6.96)
	psl	1007.53	−0.08 (−1.16~0.98)	0.63 (0.59~1.43)
	pr	5.77	−0.09 (−1.11~1.13)	2.74 (2.81~3.74)
	evspsbl	0.000033	0.000002 (−0.000002~0.000007)	0.000008 (0.000007~0.000013)
	uas	−0.01	0.22 (0.09~0.31)	0.95 (0.93~1.11)
	vas	0.90	0.25 (0.21~0.28)	0.78 (0.77~1.01)
	sfcWindmax	6.84	0.40 (0.22~0.54)	1.04 (1.00~1.17)
	sfcWind	3.95	0.76 (0.70~0.83)	1.02 (1.00~1.07)
	ua850	1.82	−0.02 (−0.08~0.03)	0.67 (0.62~0.75)
	va850	1.54	−0.07 (−0.16~0.01)	0.92 (0.85~1.14)
	ta850	17.73	0.29 (−0.20~0.68)	0.61 (0.58~0.87)
	hus850	0.010555	0.000043 (−0.000567~0.000509)	0.000713 (0.000764~0.001374)

Figure 4 displays a heatmap of TSS calculated for each ensemble member and the EM across seasons and variables. All ensemble members and the EM achieved TSS values

above 0.7, indicating strong overall simulation fidelity. Consistent with the findings in Figure 3, lower performance was confirmed for hfss and vas, with TSS values ranging from approximately 0.74 to 0.83 and 0.73 to 0.87, respectively. Seasonal performance analysis showed that simulation skill was highest in winter, whereas autumn exhibited relatively lower scores for specific variables (hfss, uas, vas, va850), with TSS values ranging from approximately 0.71 to 0.93. Inter-member comparisons revealed that members employing the MYJ PBL scheme (ENS02, ENS04, ENS06, and ENS08) exhibited lower performance than those using the YSU PBL scheme (ENS01, ENS03, ENS05, and ENS07). In particular, ENS02 displayed noticeably reduced skill for variables such as hfss, pr, and vas.

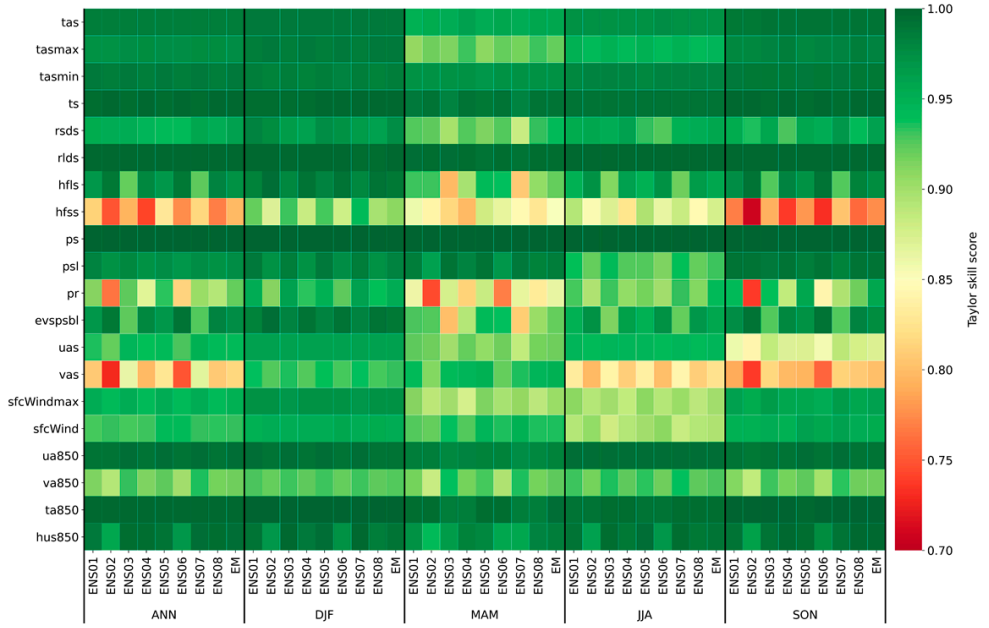


Figure 4. Heatmap of the Taylor skill scores for the evaluated variables. Rows correspond to the evaluated variables, and columns are grouped by season (ANN, DJF, MAM, JJA and SON) and ensemble member (ENS01–ENS08 and EM).

To quantify the impact of physics scheme selection on simulation variability, ANOVA was applied to calculate the variance contributions of individual physical processes (MPS, CPS, PBL), two-way interactions (MPS–CPS, MPS–PBL, CPS–PBL), and the three-way interaction (MPS–CPS–PBL) for each season and variable, presented as a heatmap in Figure 5. Overall, the contributions from individual physical processes dominated over interaction terms, with CPS and PBL selections serving as primary drivers of variability for numerous cases, including summer precipitation. However, there were also instances where the MPS served as the primary factor, such as for winter tas and tasmin. Contributions from two-way physics interactions were generally small for most variables; nevertheless, certain combinations contributed 10–30% of the variance for winter and spring surface winds (vas, sfcWindmax, sfcWind) and winter lower-tropospheric temperature (ta850), highlighting variations dependent on the variable and season. The three-way physics interaction contributed minimally across all seasons and variables, remaining below 5%.

Figure 6 presents the spatial distributions of surface air temperature over the EA region during winter and summer for OBS and the EM, along with the individual biases of the eight ensemble members relative to OBS. The EM effectively reproduces the spatial features depicted in OBS, including the poleward temperature drop with increasing

latitude across East Asia and the cold temperatures over high-elevation regions such as the Tibetan Plateau. However, in winter, individual ensemble members consistently displayed negative biases over the Tibetan Plateau, Southeast Asia, Manchuria, the Korean Peninsula, and Japan, alongside positive biases over India, regions north of the Tibetan Plateau, and Mongolia. In summer, temperature biases shifted toward more positive values relative to winter, while maintaining generally similar spatial bias patterns. Consequently, the EM exhibited domain-averaged cold biases of −1.13 °C in winter and −0.44 °C in summer relative to OBS (Table 3). Overall, the physics ensemble members exhibited consistent bias patterns relative to OBS, with domain-averaged biases ranging from −1.28 to −0.94 °C in winter and from −0.67 to −0.18 °C in summer (Table 3). This indicates that variations among physics combinations exert a relatively minor influence on spatial distributions and domain-averaged surface air temperature.

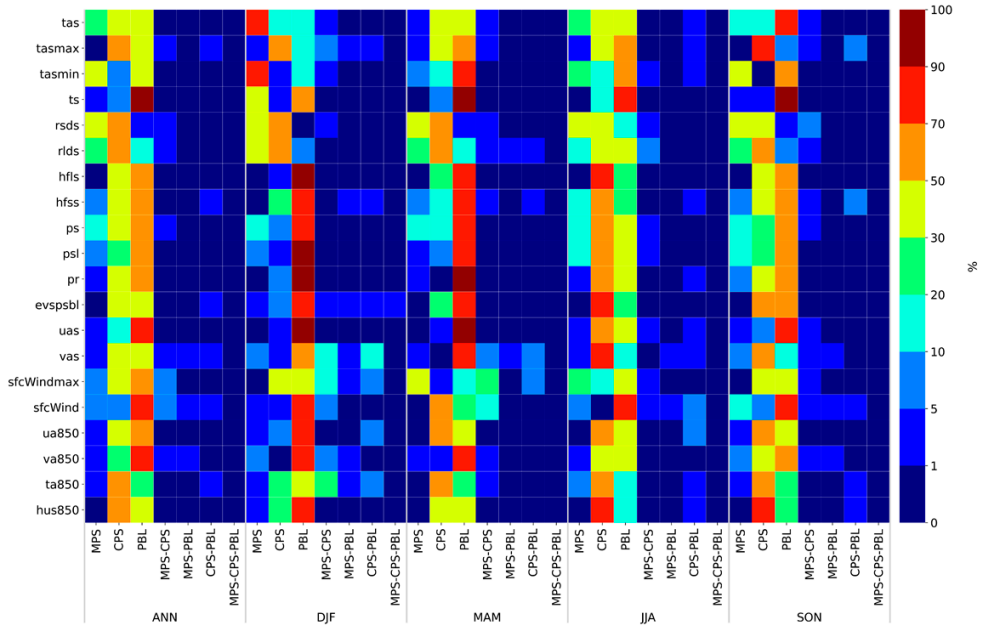


Figure 5. Heatmap of the percentage contributions of individual and interaction effects among physical parameterization schemes derived from ANOVA. Rows correspond to the evaluated variables, and columns are grouped by season (ANN, DJF, MAM, JJA and SON) and effect (MPS, CPS, PBL, MPS–CPS, MPS–PBL, CPS–PBL, and MPS–CPS–PBL).

Figure 7 presents the long-term monthly mean time series (Figure 7a) and annual cycle (Figure 7b) of surface air temperature for the domain corresponding to Figure 6. In both panels, the top subplots show absolute mean values, the middle subplots depict biases of individual ensemble members and the EM relative to OBS, and the bottom subplots illustrate inter-member anomalies relative to the EM. In Figure 7a, all ensemble members closely capture the long-term monthly time series of OBS, despite a systematic cold bias (EM bias of approximately −1.23 °C). Inter-member spreads relative to the EM ranged between approximately −0.3 and +0.3 °C. Notably, ENS02 and ENS06 consistently underestimated temperatures while ENS03 and ENS07 overestimated them relative to the EM, presenting a clear dipolar behavior. A comparison of physics combinations driving this dipolar behavior indicates that ENS02 and ENS06 share the MSKF–MYJ configuration, whereas ENS03 and ENS07 employ BMJ–YSU. This indicates that the contrast between these two CPS–PBL physics combinations primarily drives the temperature discrepancies among members. Regarding the annual cycle (Figure 7b), all ensemble members effectively captured the seasonal variation observed in OBS, despite

maintaining a persistent cold bias. Seasonal biases relative to OBS were smallest in summer and peaked during spring. Similarly, the dipolar pattern driven by the CPS–PBL physics combinations (ENS02/ENS06 vs. ENS03/ENS07) identified in Figure 7a was also evident in the inter-member anomalies relative to the EM during the annual cycle, remaining within a range of 0.6 °C.

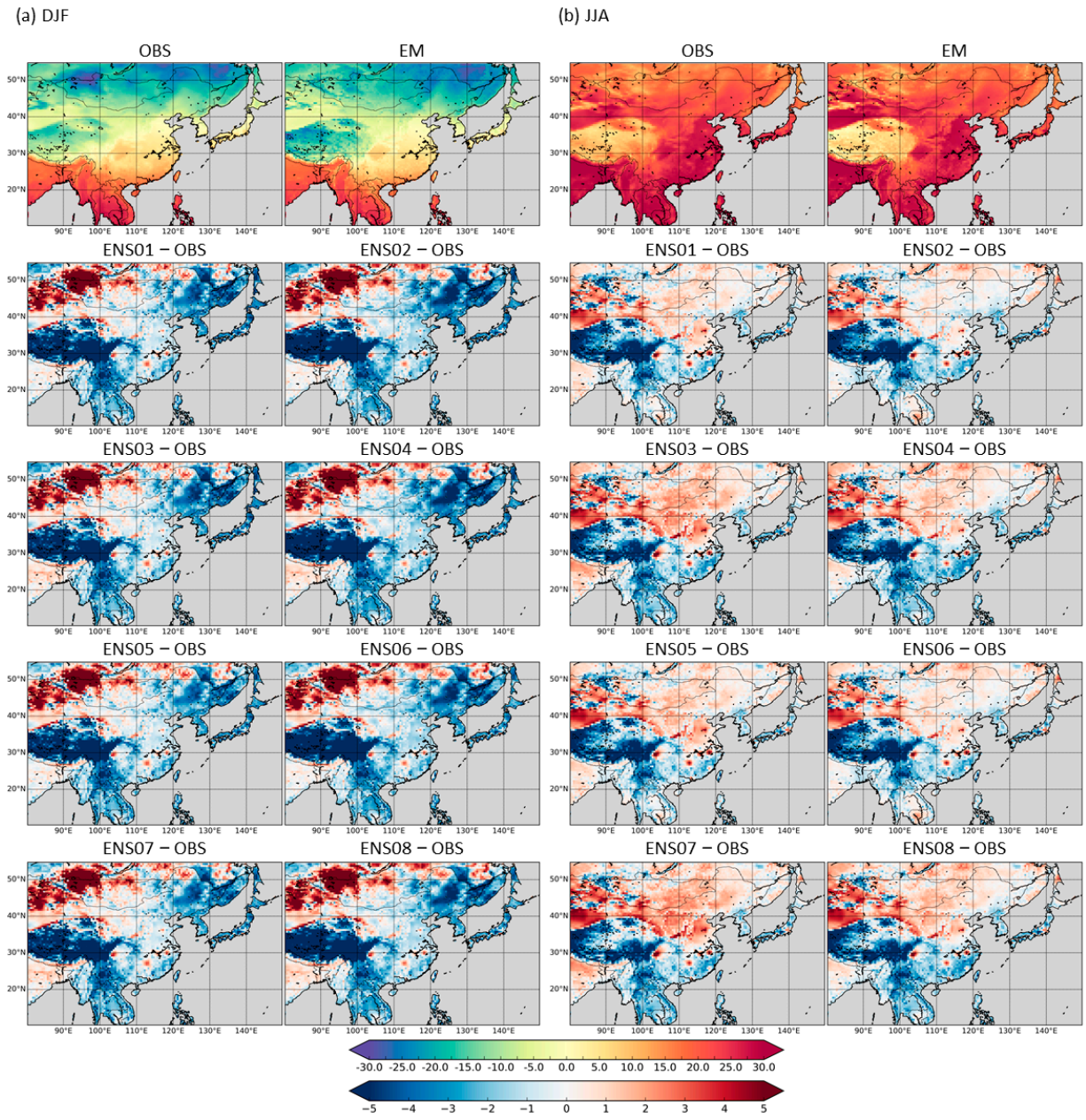


Figure 6. Spatial distributions of seasonal mean near-surface air temperature (°C) in (**a**) winter and (**b**) summer over the East Asia region. The first row shows the seasonal means of OBS and EM, while the remaining rows present the biases of individual ensemble members relative to OBS.

Figure 8 presents the spatial distributions of precipitation over the EA region during winter and summer for OBS and the EM, along with the individual biases of the eight ensemble members relative to OBS. In winter (Figure 8a), the EM effectively reproduces the spatial features depicted in OBS, including the lower precipitation amounts compared to summer and the weak rainband extending from Japan and Taiwan across the Pacific to

the Philippines. However, individual ensemble members consistently displayed negative biases over parts of inland southeastern China and oceanic regions around 30° N. In low-latitude oceanic areas, members employing the YSU PBL scheme (ENS01, ENS03, ENS05, and ENS07) overestimated precipitation relative to OBS, whereas members using the MYJ PBL scheme (ENS02, ENS04, ENS06, and ENS08) underestimated precipitation, highlighting sensitivity to the choice of PBL scheme. Differences associated with MPSs (ENS01–ENS04 vs. ENS05–ENS08) and CPSs (ENS01, ENS02, ENS05, ENS06 vs. ENS03, ENS04, ENS07, ENS08) were relatively minor in winter. In summer (Figure 8b), precipitation increases substantially across East Asia, with heavy rainfall extending into inland regions—a characteristic feature well captured by the EM. Nevertheless, individual member biases relative to OBS shared common tendencies, including general overestimation over inland areas and underestimation over the Bay of Bengal, with larger bias magnitudes over oceanic regions than land. Inter-member comparisons showed that YSU PBL members (ENS01, ENS03, ENS05, and ENS07) simulated higher precipitation than MYJ PBL members (ENS02, ENS04, ENS06, and ENS08). For the CPS, MSKF members (ENS01, ENS02, ENS05, and ENS06) simulated less oceanic precipitation than BMJ members (ENS03, ENS04, ENS07, and ENS08). For the MPS, members employing P3 (ENS05–ENS08) produced slightly higher oceanic precipitation than those using WSM6 (ENS01–ENS04). Notably, low-latitude oceanic precipitation biases varied substantially depending on the CPS and PBL selection: the CPS–BMJ and PBL–YSU combination (ENS03 and ENS07) simulated relatively higher precipitation, whereas the CPS–MSKF and PBL–MYJ combination (ENS02 and ENS06) produced lower precipitation. However, over the region spanning Shandong to Jilin in China, ENS03 and ENS07 underestimated precipitation while ENS02 and ENS06 overestimated it, displaying a pattern opposite to that observed in low-latitude oceanic regions.

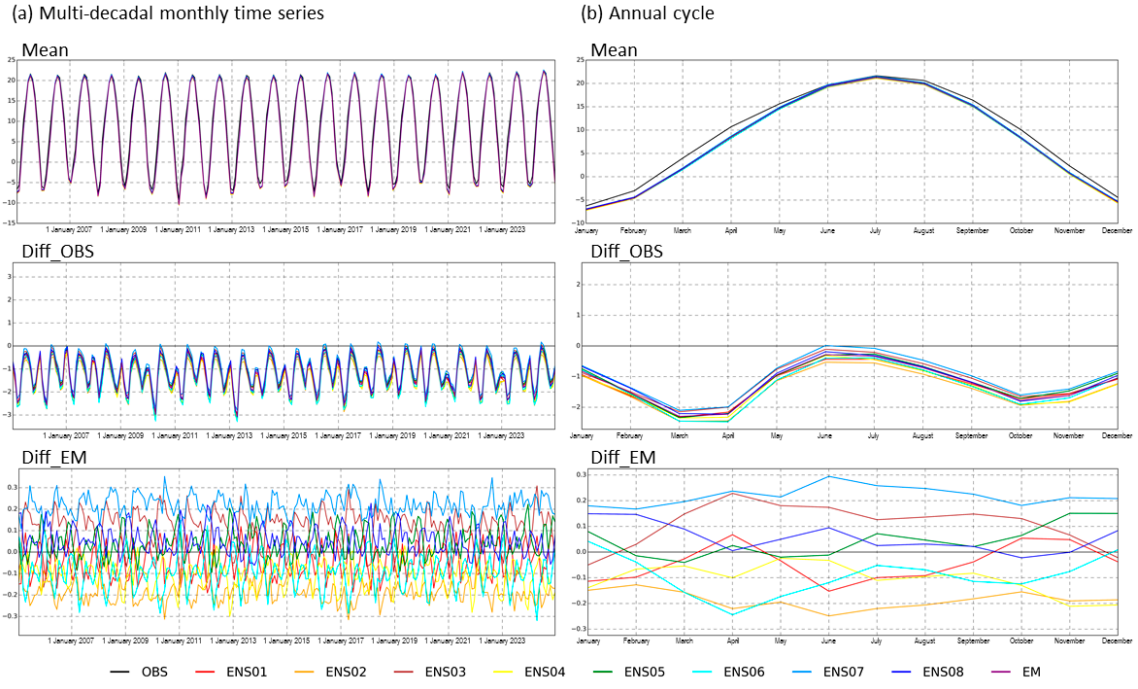


Figure 7. Multi-decadal monthly time series (**a**) and annual cycle (**b**) of near-surface air temperature (°C) over the East Asia region. The top row shows the OBS and EM values, the middle row presents biases of individual ensemble members and the EM relative to OBS, and the bottom row shows inter-member anomalies relative to the EM.

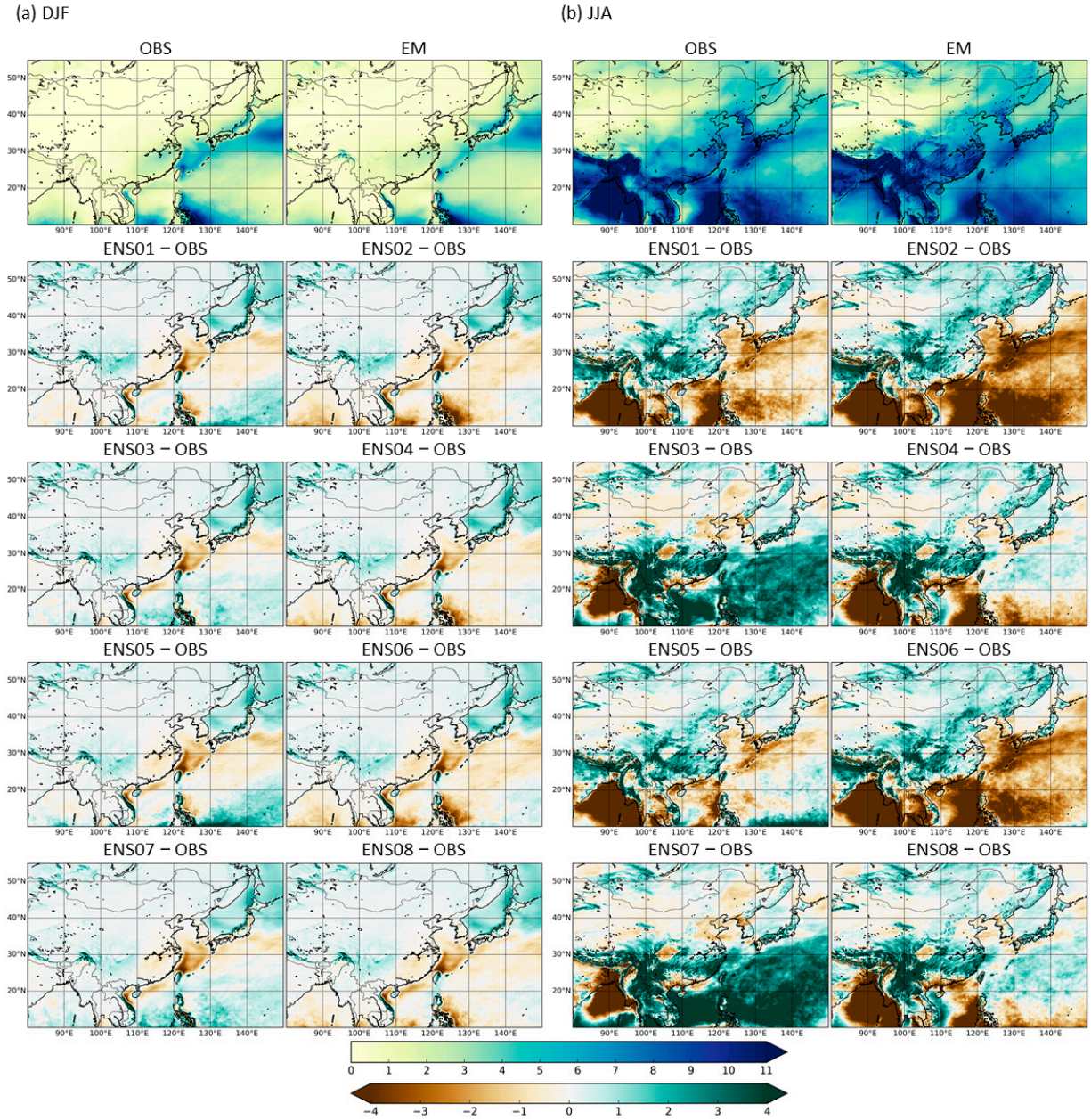


Figure 8. Same as Figure 6, except for precipitation (mm day^{-1}).

Figure 9 presents the long-term monthly mean time series (Figure 9a) and annual cycle (Figure 9b) of precipitation for the domain corresponding to Figure 8. As in the temperature analysis (Figure 7), in both panels, the top subplots show absolute mean values, the middle subplots depict biases of individual ensemble members and the EM relative to OBS, and the bottom subplots illustrate inter-member anomalies relative to the EM. All ensemble members generally capture the temporal evolution and annual cycle of East Asian precipitation, exhibiting smaller biases in winter and larger biases in summer. Inter-member spreads relative to OBS and the EM remain small during winter across all subplots. However, from spring to autumn, members employing the CPS–BMJ and PBL–YSU combination (ENS03 and ENS07) consistently overestimated precipitation relative to OBS, whereas members with the CPS–MSKF and PBL–MYJ combination (ENS02 and ENS06) underestimated it. This contrast is clearly reflected in the inter-member anomalies relative to the EM (bottom subplots), where ENS03 and ENS07 displayed positive

anomalies (ranging from approximately 0.5 to 1.5 mm day^{-1}) while ENS02 and ENS06 exhibited negative anomalies (ranging from approximately −1.3 to −0.5 mm day^{-1}), demonstrating a pronounced dipolar pattern. These results reaffirm that the choice of CPS and PBL physics schemes plays a crucial role in simulating summer precipitation over East Asia, consistent with the findings in Figures 5 and 8.

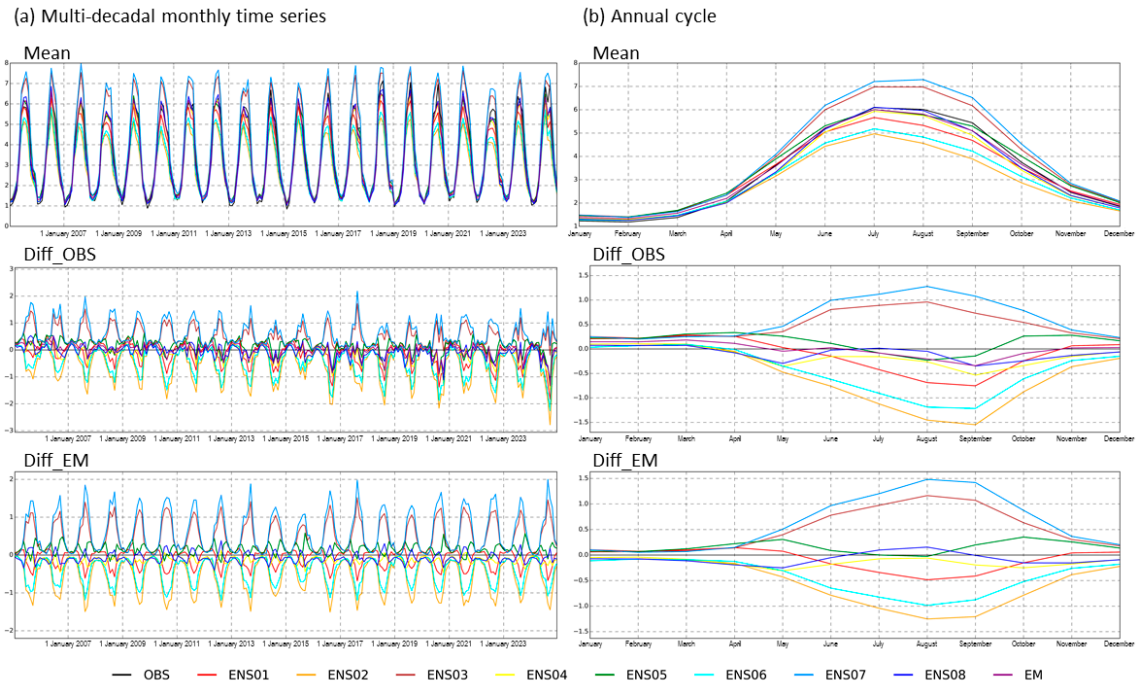


Figure 9. Same as Figure 7, except for precipitation (mm day^{-1}).

To further investigate the inter-member summer precipitation discrepancies, we analyzed the spatial distributions of lower-tropospheric (850 hPa) wind and specific humidity over the EA region during summer (Figure 10). Because the observational datasets used previously (CPC and IMERG) do not provide 850 hPa variables, ERA5 reanalysis was utilized as the reference dataset (OBS). The EM effectively reproduced the general spatial features of summer 850 hPa specific humidity and wind fields, showing strong agreement with OBS. However, examination of individual ensemble members revealed common bias tendencies: all members simulated excessively strong southward flow south of 20° N and strong northward flow north of 30° N. Over the region extending from southeastern China through Shandong to Jilin, members employing the CPS–BMJ and PBL–YSU combination (ENS03 and ENS07) displayed small wind biases, whereas members with the CPS–MSKF and PBL–MYJ combination (ENS02 and ENS06) simulated excessively strong southerly winds. For specific humidity, over oceanic regions where the Western North Pacific Subtropical High (WNPSH) is situated during summer, members employing the CPS–MSKF scheme (ENS01, ENS02, ENS05, and ENS06) tended to exhibit negative biases, whereas those using the CPS–BMJ scheme (ENS03, ENS04, ENS07, and ENS08) showed positive biases. This contrast was particularly pronounced in ENS02/ENS06 (negative biases) and ENS03/ENS07 (positive biases). Synthesizing these lower-tropospheric wind and moisture characteristics with the summer precipitation results in Figure 8 indicates that the oceanic precipitation biases driven by CPS–PBL combinations are closely tied to lower-tropospheric specific humidity and circulation anomalies. Furthermore, precipitation biases over the Shandong–Jilin region appear to be

driven by inter-member discrepancies in simulating the intensity of southerly winds that transport moisture from lower latitudes.

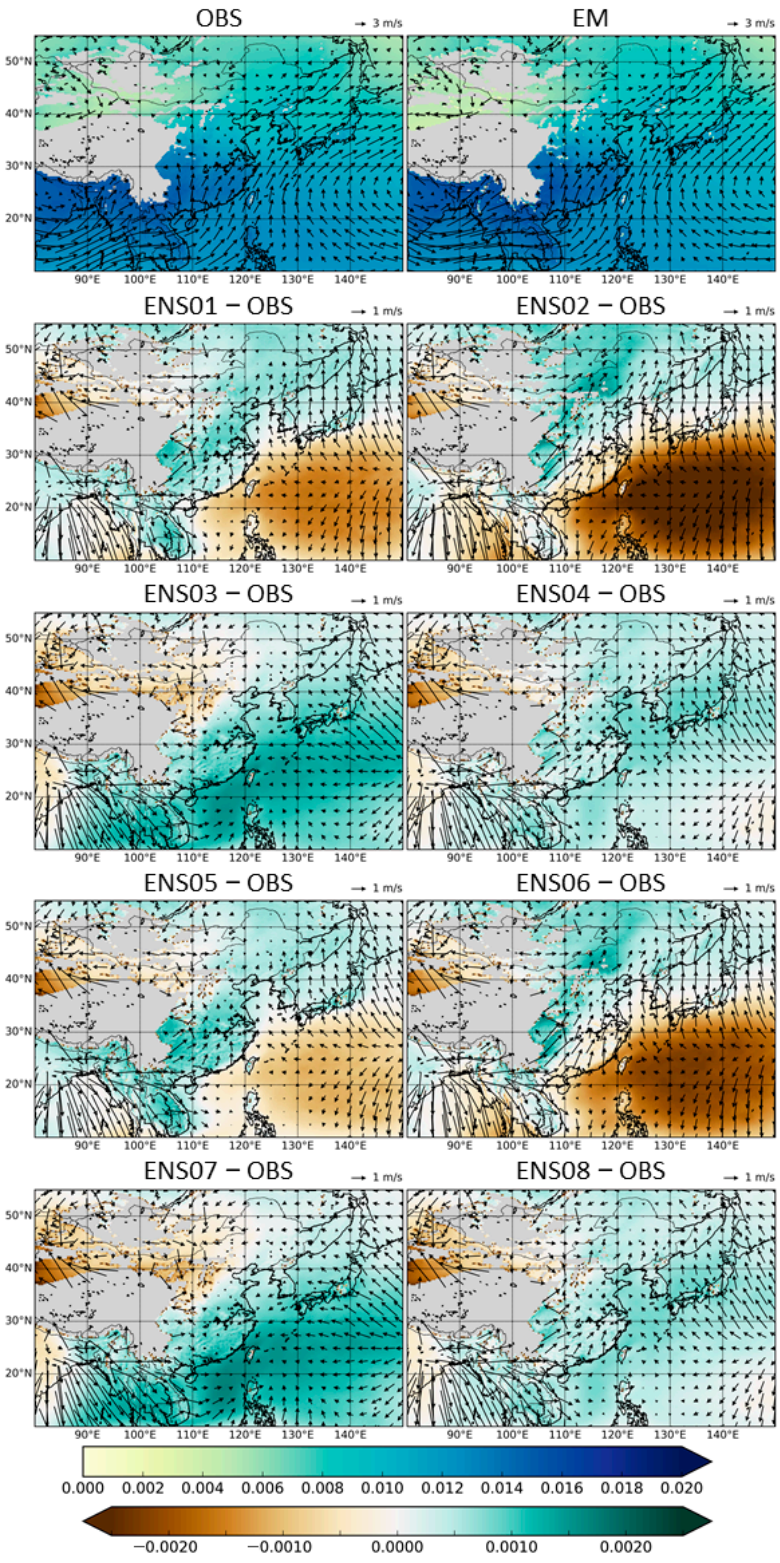


Figure 10. Spatial distributions of summer (JJA) mean 850 hPa wind vectors and specific humidity (shaded) over the East Asia region. The first row shows the OBS and the EM, while the remaining rows present the biases of individual ensemble members relative to OBS.

https://doi.org/10.3390/atmos17111118

4. Discussion

Evaluation of model performance using Taylor diagrams and Taylor skill scores demonstrated that both the EM and individual physics ensemble members generally exhibited high simulation skill. However, the simulation performance was not uniformly high across all evaluations; instead, substantial variations were observed depending on the variable, season, and physics combination. Furthermore, mean bias, which is not captured in Taylor diagrams, remains a crucial factor to be considered. These findings are consistent with earlier studies comparing diverse physics configurations [38–40]. Specific variables such as hfss, pr, and vas showed lower fidelity relative to others, and skill was generally lower in non-winter seasons compared to winter.

ANOVA results further revealed that CPS and PBL selections served as the primary drivers of inter-member variability across most variables, whereas the impact of MPS selection was relatively minor. Contributions from two- and three-way physics interactions remained low across most variables. It should be noted that these ANOVA results quantify the relative influence of physics schemes on the inter-member spread (simulation uncertainty), rather than reflecting agreement with observations.

Additionally, while ERA5 was employed as reference data due to the lack of observational datasets covering diverse variables, evaluations against it do not constitute a completely independent validation because ERA5 also provided the boundary forcing. Nevertheless, this analysis was conducted primarily for the purpose of establishing a rationale for the future utilization of the produced variables.

Furthermore, additional analyses were conducted to compare the spatiotemporal bias distributions of surface air temperature and precipitation across physics ensemble members. All ensemble members effectively reproduced the spatial temperature patterns depicted in OBS during both winter and summer, exhibiting generally consistent spatial bias characteristics. The similarity in bias distributions among members suggests that shared components—such as the land surface model, radiation schemes, land use data, and driving initial/boundary conditions held constant in this study—may exert a substantial influence on the baseline simulation results. Previous studies have demonstrated that altering the land surface model, radiation schemes, resolution, or lateral boundary forcing can lead to different regional climate simulations [41–44]. A similar tendency was observed in the long-term monthly time series and annual cycle, where ensemble members captured overall temporal variability well despite maintaining a systematic cold bias relative to OBS. Regarding inter-member anomalies relative to the EM, ENS02 and ENS06 (employing the CPS–MSKF and PBL–MYJ combination) underestimated temperatures, whereas ENS03 and ENS07 (using the CPS–BMJ and PBL–YSU combination) overestimated them, highlighting a distinct dipolar behavior driven by the choice of physics combinations.

For precipitation, all ensemble members similarly captured the spatial distributions and temporal patterns relative to OBS in both winter and summer. However, particularly during summer, ENS02 and ENS06 underestimated precipitation, whereas ENS03 and ENS07 overestimated it. As indicated by the spatial distribution results, these discrepancies largely stem from variations in simulating precipitation over the Western North Pacific depending on the CPS–PBL combination, reaffirming the critical role of CPS and PBL selections in East Asian precipitation modeling. Nevertheless, because certain subregions exhibit bias responses opposite to the domain-averaged tendency, selecting physics combinations tailored to specific target regions remains essential.

However, numerous studies have highlighted that simulation performance can vary depending on the chosen experimental domain and target evaluation region [45–48]. Therefore, to support climate change research applications in Korea, an additional performance evaluation was conducted over the Korean Peninsula domain, with results

provided in the Supplementary Materials. Compared to the domain-wide evaluation over East Asia, simulation skill assessed via Taylor diagrams and Taylor skill scores exhibited substantial differences across variables and ensemble members over the Korean Peninsula (Figures S1 and S2). Furthermore, while bias time series for surface air temperature and precipitation displayed persistent, distinct inter-member tendencies over East Asia, bias patterns over the Korean Peninsula underwent shifts during late summer to autumn for temperature and during summer for precipitation (Figures S4 and S6). These findings confirm that the sensitivity of simulated temperature and precipitation to physics combinations varies depending on the target analysis region. Therefore, the findings regarding physics scheme sensitivities in this study should not be overly generalized, as they are inherently dependent on the chosen regional model, experimental domain, and simulation period.

5. Conclusions

This study constructed eight ensemble members by combining two distinct schemes for each of the MPS, CPS, and PBL options in the WRF model. Driven by ERA5 reanalysis data for initial and boundary conditions, 12 km horizontal resolution simulations were conducted over the CORDEX-EA Phase 2 domain to evaluate the simulation fidelity of individual ensemble members and the EM.

Overall, the multi-physics ensemble effectively reproduced historical spatial patterns and seasonal cycles, with CPS and PBL selections acting as the primary drivers of inter-member spread and exhibiting distinct dipolar bias behaviors over East Asia. However, simulation performance varied noticeably depending on the variable, season, and physics combination, with marked differences also observed between the East Asia domain and the Korean Peninsula.

This study holds key significance in presenting quantitative evaluation metrics for a broad range of climate variables required across diverse disciplines by executing WRF simulations with multiple physics combinations based on the recommended CORDEX experimental framework. Furthermore, by establishing the simulation performance of individual physics combinations, this work provides a valuable scientific foundation for interpreting future climate change projections over East Asia and the Korean Peninsula.

Supplementary Materials: The following supporting information can be downloaded at https://www.mdpi.com/article/10.3390/atmos17111118/s1, Figure S1: Taylor diagrams showing the performance of individual ensemble members (ENS01–ENS08) and the EM relative to OBS for (a) annual (ANN), (b) DJF, (c) MAM, (d) JJA, and (e) SON using normalized standard deviation and spatial correlation. The color and number assigned to each point are indicated in the legend; Figure S2: Heatmap of the Taylor skill scores for the evaluated variables. Rows correspond to the evaluated variables, and columns are grouped by season (ANN, DJF, MAM, JJA and SON) and ensemble member (ENS01-ENS08 and EM); Figure S3: Spatial distributions of seasonal mean near-surface air temperature (°C) in (a) winter and (b) summer over the Korean Peninsula region. The top-left and bottom-left subplots show the seasonal means of OBS and EM, respectively. The remaining subplots present the biases of individual ensemble members relative to OBS (ENS01-ENS04 in the top row and ENS05-ENS08 in the bottom row); Figure S4: Multi-decadal monthly time series (a) and annual cycle (b) of near-surface air temperature (°C) over the Korean Peninsula region. The top row shows the OBS and EM values, the middle row presents the biases of individual ensemble members and the EM relative to OBS, and the bottom row shows inter-member anomalies relative to the EM; Figure S5: same as Figure S3, except for precipitation (mm day^{-1}); Figure S6: same as Figure S4, except for precipitation (mm day^{-1}); Table S1: DJF statistics for each variable over the Korean Peninsula: observation (OBS) mean, ensemble mean (EM) bias and RMSE. Values in parentheses

indicate the minimum–maximum range among ensemble members; Table S2: same as Table S1, except for JJA.

Author Contributions: Conceptualization, T.-J.K., J.-U.K., J.-K.S., K.-O.B., S.-K.M., D.-H.C. and E.-C.C.; methodology, T.-J.K., J.-U.K., J.-K.S., K.-O.B., S.-K.M., D.-H.C. and E.-C.C.; software, T.-J.K., S.-K.M., D.-H.C. and E.-C.C.; validation, T.-J.K., J.-U.K., J.-K.S., M.-J.C. and K.-O.B.; formal analysis, T.-J.K.; investigation, T.-J.K. and M.-J.C.; data curation, T.-J.K. and M.-J.C.; writing—original draft preparation, T.-J.K. and J.-U.K.; writing—review and editing, T.-J.K., J.-U.K., J.-K.S., M.-J.C., K.-O.B., S.-K.M., D.-H.C. and E.-C.C.; visualization, T.-J.K.; supervision, K.-O.B.; project administration, J.-U.K., J.-K.S. and K.-O.B. All authors have read and agreed to the published version of the manuscript.

Funding: This work was funded by the Korea Meteorological Administration Research and Development Program "Developing and Assessing Climate Change Scenarios" under grant (KMA2018-00321).

Institutional Review Board Statement: Not applicable.

Informed Consent Statement: Not applicable.

Data Availability Statement: The CPC global temperature data, IMERG V07 precipitation data, and ERA5 reanalysis data used in this study are publicly available from the NCEP/Climate Prediction Center, NASA Global Precipitation Measurement (GPM) mission, and Copernicus Climate Change Service (C3S) Climate Data Store, respectively.

Conflicts of Interest: The authors declare no conflicts of interest.

Abbreviations

The following abbreviations are used in this manuscript:

ANOVA	Analysis of variance
AR5	Fifth Assessment Report
AR6	Sixth Assessment Report
AR7	Seventh Assessment Report
BMJ	Betts–Miller–Janjić
CPC	Climate Prediction Center
CPS	Cumulus parameterization scheme
CORDEX	Coordinated Regional Climate Downscaling Experiment
EA	East Asia
ECMWF	European Center for Medium-Range Weather Forecasts
EM	Ensemble mean
ENS	Ensemble
ERA5	Fifth-generation ECMWF reanalysis
GCM	Global Climate Model
IMERG	Integrated Multi-satellitE Retrievals for GPM
IPCC	Intergovernmental Panel on Climate Change
KMA	Korea Meteorological Administration
MPS	Microphysics scheme
MSKF	Multi-Scale Kain–Fritsch
MYJ	Mellor–Yamada–Janjić
NCAR	National Center for Atmospheric Research
NIMS	National Institute of Meteorological Sciences
OBS	Observation
P3	Predicted Particle Properties
PBL	Planetary boundary layer
RCM	Regional Climate Model
RMSE	Root Mean Square Error
RRTMG	Rapid Radiative Transfer Model for GCMs

TKE	Turbulent Kinetic Energy
TSS	Taylor skill score
WCRP	World Climate Research Program
WNPSH	Western North Pacific Subtropical High
WRF	Weather Research and Forecasting
WSM6	WRF Single-Moment 6-class microphysics scheme
YSU	Yonsei University

References

1. IPCC. Summary for policymakers. In *Climate Change 2023: Synthesis Report. Contribution of Working Groups I, II and III to the Sixth Assessment Report of the Intergovernmental Panel on Climate Change*; Core Writing Team, Lee, H., Romero, J., Eds.; IPCC: Geneva, Switzerland, 2023. https://doi.org/10.59327/IPCC/AR6-9789291691647.001.
2. Oh, S.-G.; Park, J.-H.; Lee, S.-H.; Suh, M.-S. Assessment of the RegCM4 over East Asia and future precipitation change adapted to the RCP scenarios. *J. Geophys. Res. Atmos.* **2014**, *119*, 2913–2927. https://doi.org/10.1002/2013JD020693.
3. Giorgi, F.; Gutowski, W.J. Coordinated experiments for projections of regional climate change. *Curr. Clim. Change Rep.* **2016**, *2*, 202–210. https://doi.org/10.1007/s40641-016-0046-6.
4. Haarsma, R.J.; Roberts, M.J.; Vidale, P.L.; Senior, C.A.; Bellucci, A.; Bao, Q.; Chang, P.; Corti, S.; Fučkar, N.S.; Guemas, V.; et al. High Resolution Model Intercomparison Project (HighResMIP v1.0) for CMIP6. *Geosci. Model Dev.* **2016**, *9*, 4185–4208. https://doi.org/10.5194/gmd-9-4185-2016.
5. Giorgi, F. Thirty years of regional climate modeling: Where are we and where are we going next? *J. Geophys. Res. Atmos.* **2019**, *124*, 5696–5723. https://doi.org/10.1029/2018JD030094.
6. Gu, H.; Yu, Z.; Yang, C.; Ju, Q.; Yang, T.; Zhang, D. High-resolution ensemble projections and uncertainty assessment of regional climate change over China in CORDEX East Asia. *Hydrol. Earth Syst. Sci.* **2018**, *22*, 3087–3103. https://doi.org/10.5194/hess-22-3087-2018.
7. Yu, K.; Hui, P.; Zhou, W.; Tang, J. Evaluation of multi-RCM high-resolution hindcast over the CORDEX East Asia Phase II region: Mean, annual cycle and interannual variations. *Int. J. Climatol.* **2019**, *40*, 2134–2152. https://doi.org/10.1002/joc.6323.
8. Fu, C.; Wang, S.; Xiong, Z.; Gutowski, W.J.; Lee, D.K.; McGregor, J.L.; Sato, Y.; Kato, H.; Kim, J.W.; Suh, M.S. Regional climate model intercomparison project (RMIP) for Asia. *Bull. Am. Meteorol. Soc.* **2005**, *86*, 257–266. https://doi.org/10.1175/BAMS-86-2-257.
9. Bellprat, O.; Kotlarski, S.; Lüthi, D.; Schär, C. Exploring perturbed physics ensembles in a regional climate model. *J. Clim.* **2012**, *25*, 4582–4599. https://doi.org/10.1175/JCLI-D-11-00275.1.
10. Li, P.; Niu, X.; Mao, Y.; Wu, R.; Ling, X. Assessment of climate simulation over the Tibetan Plateau based on high-resolution multi-RCM within CORDEX-EA-II. *Atmos. Res.* **2023**, *292*, 106848. https://doi.org/10.1016/j.atmosres.2023.106848.
11. Giorgi, F.; Jones, C.; Asrar, G.R. Addressing climate information needs at the regional level: The CORDEX framework. *WMO Bull.* **2009**, *58*, 175–183.
12. Gutowski, W.J.; Giorgi, F.; Timbal, B.; Frigon, A.; Jacob, D.; Kang, H.S.; Raghavan, K.; Lee, B.; Lennard, C.; Nikulin, G.; et al. WCRP Coordinated Regional Downscaling Experiment (CORDEX): A diagnostic MIP for CMIP6. *Geosci. Model Dev.* **2016**, *9*, 4087–4095. https://doi.org/10.5194/gmd-9-4087-2016.
13. Van Vuuren, D.P.; O'Neill, B.C.; Tebaldi, C.; Sanderson, B.M.; Chini, L.P.; Friedlingstein, P.; Hasegawa, T.; Riahi, K.; Govindasamy, B.; Bauer, N.; et al. The Scenario Model Intercomparison Project for CMIP7 (ScenarioMIP-CMIP7). *Geosci. Model Dev.* **2026**, *19*, 2627–2656. https://doi.org/10.5194/gmd-19-2627-2026.
14. Fernandez, J.; Buntemeyer, L.; Nikulin, G.; MCGinnis, S.; Teichmann, C.; Cavazos, T.; Brands, S.; Nabat, P.; Paquin, D.; Thatcher, M.; et al. CORDEX Task Force report on proposed actions, steps and timelines in preparation for CORDEX-CMIP7. *Zenodo* **2025**. https://doi.org/10.5281/zenodo.17821547.
15. Kim, J.-U.; Kim, T.-J.; Shim, J.-K.; Chung, C.-Y.; Kim, D.-H.; Boo, K.-O.; Min, S.-K.; Cha, D.-H.; Chang, E.-C.; Shim, S. Development of a next-generation regional climate scenario system toward IPCC AR7 for East Asia. *J. Clim. Change Res.* **2025**, *16*, 1047–1060. https://doi.org/10.15531/KSCCR.2025.16.5.1047.
16. Kim, J.-U.; Kim, T.-J.; Kim, D.-H.; Byun, Y.-H.; Chang, E.-C.; Cha, D.-H.; Ahn, J.-B.; Min, S.-K. Performance Evaluation and Future Projection of East Asian Climate using SSP scenario-based CORDEX-East Asia Phase 2 Multi-RCM Simulations. *J. Clim. Change Res.* **2022**, *13*, 339–354. https://doi.org/10.15531/KSCCR.2022.13.3.339.

17. Seo, G.-Y.; Ahn, J.-B.; Cha, D.-H.; Suh, M.-S.; Min, S.-K.; Chang, E.-C.; Byun, Y.-H.; Kim, J.-U. Evaluation of multi-RCM ensembles for simulating spatiotemporal variability of Asian summer monsoon precipitation in the CORDEX-East Asia Phase 2 domain. *Int. J. Climatol.* **2023**, *43*, 3710–3729. https://doi.org/10.1002/joc.8054.
18. Kim, E.; Kim, T.; Mun, T.; Shin, S.-W.; Lee, M.; Cha, D.-H.; Chang, E.-C.; Ahn, J.-B.; Min, S.-K.; Kim, J.-U.; et al. Multimodel GCM-RCM ensemble-based projections of tropical cyclone activities over CORDEX East Asia domain. *Clim. Dyn.* **2025**, *63*, 143. https://doi.org/10.1007/s00382-025-07627-6.
19. Giorgi, F.; Coppola, E.; Jacob, D.; Teichmann, C.; Abba Omar, S.; Ashfaq, M.; Ban, N.; Bülow, K.; Bukovsky, M.; Buntemeyer, L.; et al. The CORDEX-CORE EXP-I Initiative: Description and Highlight Results from the Initial Analysis. *Bull. Am. Meteorol. Soc.* **2022**, *103*, E293–E310. https://doi.org/10.1175/BAMS-D-21-0119.1.
20. Skamarock, W.C.; Klemp, J.B.; Dudhia, J.; Gill, D.O.; Liu, Z.; Berner, J.; Wang, W.; Powers, J.G.; Duda, M.G.; Barker, D.M.; et al. *A Description of the Advanced Research WRF Model Version 4*; NCAR Technical Note NCAR/TN-556+STR; NSF National Center for Atmospheric Research: Boulder, CO, USA, 2019; 145p. https://doi.org/10.5065/1dfh-6p97.
21. Skamarock, W.C.; Klemp, J.B.; Dudhia, J.; Gill, D.O.; Barker, D.M.; Duda, M.G.; Huang, X.-Y.; Wang, W.; Powers, J.G. *A Description of the Advanced Research WRF Version 3*; NCAR Technical Note NCAR/TN-475+STR; NSF National Center for Atmospheric Research: Boulder, CO, USA, 2008. https://doi.org/10.5065/D68S4MVH.
22. Di, Z.; Duan, Q.; Gong, W.; Wang, C.; Gan, Y.; Quan, J.; Li, J.; Miao, C.; Ye, A.; Tong, C. Assessing WRF model parameter sensitivity: A case study with 5 day summer precipitation forecasting in the Greater Beijing Area. *Geophys. Res. Lett.* **2015**, *42*, 579–587. https://doi.org/10.1002/2014GL061623.
23. Argüeso, D.; Hidalgo-Muñoz, J.M.; Gámiz-Fortis, S.R.; Esteban-Parra, M.J.; Dudhia, J.; Castro-Díez, Y. Evaluation of WRF parameterizations for climate studies over Southern Spain using a multistep regionalization. *J. Clim.* **2011**, *24*, 5633–5651. https://doi.org/10.1175/JCLI-D-11-00073.1.
24. Evans, J.P.; Ekström, M.; Ji, F. Evaluating the performance of a WRF physics ensemble over South-East Australia. *Clim. Dyn.* **2012**, *39*, 1241–1258. https://doi.org/10.1007/s00382-011-1244-5.
25. Liu, S. Sensitivity of WRF-simulated 2m temperature and precipitation to physics options over the Loess Plateau. *Adv. Meteorol.* **2024**, *2024*, 1–15. https://doi.org/10.1155/2024/6633255.
26. Tewari, M.; Chen, F.; Wang, W.; Dudhia, J.; LeMone, M.A.; Mitchell, K.; Ek, M.; Gayno, G.; Wegiel, J.; Cuenca, R.H. Implementation and verification of the unified NOAH land surface model in the WRF model. In Proceedings of the 20th Conference on Weather Analysis and Forecasting/16th Conference on Numerical Weather Prediction, Seattle, WA, USA, 12–16 January 2004; pp. 11–15.
27. Iacono, M.J.; Delamere, J.S.; Mlawer, E.J.; Shephard, M.W.; Clough, S.A.; Collins, W.D. Radiative forcing by long-lived greenhouse gases: Calculations with the AER radiative transfer models. *J. Geophys. Res.* **2008**, *113*, D13103. https://doi.org/10.1029/2008JD009944.
28. Hersbach, H.; Bell, B.; Berrisford, P.; Hirahara, S.; Horányi, A.; Muñoz-Sabater, J.; Nicolas, J.; Peubey, C.; Radu, R.; Schepers, D.; et al. The ERA5 global reanalysis. *Q. J. R. Meteorol. Soc.* **2020**, *146*, 1999–2049. https://doi.org/10.1002/qj.3803.
29. Hong, S.-Y.; Lim, J.-O.J. The WRF Single-Moment 6-Class microphysics scheme (WSM6). *J. Korean Meteorol. Soc.* **2006**, *42*, 129–151.
30. Morrison, H.; Milbrandt, J.A. Parameterization of cloud microphysics based on the prediction of bulk ice particle properties. Part 1: Scheme description and idealized tests. *J. Atmos. Sci.* **2015**, *72*, 287–311. https://doi.org/10.1175/JAS-D-14-0065.1.
31. Zheng, Y.; Alapaty, K.; Herwehe, J.A.; Del Genio, A.D.; Niyogi, D. Improving high-resolution weather forecasts using the Weather Research and Forecasting (WRF) model with an updated Kain-Fritsch scheme. *Mon. Weather Rev.* **2016**, *144*, 833–860. https://doi.org/10.1175/MWR-D-15-0005.1.
32. Janjić, Z.I. The Step–Mountain Eta Coordinate Model: Further developments of the convection, viscous sublayer, and turbulence closure schemes. *Mon. Weather Rev.* **1994**, *122*, 927–945.
33. Hong, S.-Y.; Noh, Y.; Dudhia, J. A new vertical diffusion package with an explicit treatment of entrainment processes. *Mon. Weather Rev.* **2006**, *134*, 2318–2341. https://doi.org/10.1175/MWR3199.1.
34. Taylor, K.E. Summarizing multiple aspects of model performance in a single diagram. *J. Geophys. Res. Atmos.* **2001**, *106*, 7183–7192. https://doi.org/10.1029/2000JD900719.
35. Yip, S.; Ferro, C.A.T.; Stephenson, D.B.; Hawkins, E. A simple, coherent framework for partitioning uncertainty in climate predictions. *J. Clim.* **2011**, *24*, 4634–4643. https://doi.org/10.1175/2011JCLI4085.1.
36. Fan, Y.; van den Dool, H. A global monthly land surface air temperature analysis for 1948-present. *J. Geophys. Res. Atmos.* **2008**, *113*, D01103. https://doi.org/10.1029/2007JD008470.

37. Huffman, G.J.; Bolvin, D.T.; Braithwaite, D.; Hsu, K.; Joyce, R.; Kidd, C.; Nelkin, E.J.; Sorooshian, S.; Stocker, E.F.; Tan, J.; et al. Integrated Multi-satellite Retrievals for the Global Precipitation Measurement (GPM) mission (IMERG). In *Satellite Precipitation Measurement*; Levizzani, V., Kidd, C., Kirschbaum, D.B., Kummerow, C.D., Nakamura, K., Turk, F.J., Eds.; Springer International Publishing: Cham, Switzerland, 2020; Volume 1, pp. 343–353. https://doi.org/10.1007/978-3-030-24568-9_19.
38. Shen, W.; Song, J.; Liu, G.; Zhuang, Y.; Wang, Y.; Tang, J. The effect of convection scheme on tropical cyclones simulations over the CORDEX East Asia domain. *Clim. Dyn.* **2019**, *52*, 4695–4713. https://doi.org/10.1007/s00382-018-4405-y.
39. Yang, L.; Wang, S.; Tang, J.; Niu, X.; Fu, C. Evaluation of the effects of a Multiphysics ensemble on the simulation of an extremely hot summer in 2003 over the CORDEX-EA-II region. *Int. J. Climatol.* **2019**, *39*, 3413–3430. https://doi.org/10.1002/joc.6028.
40. Niu, X.; Tang, J.; Chen, D.; Wang, S.; Ou, T.; Fu, C. The performance of CORDEX-EA-II simulations in simulating seasonal temperature and elevation-dependent warming over the Tibetan Plateau. *Clim. Dyn.* **2021**, *57*, 1135–1153. https://doi.org/10.1007/s00382-021-05760-6.
41. Hui, P.; Li, Y.; Chen, Y.; Zhang, L.; Wei, F.; Wang, S. The impact of radiation parameterization schemes on the regional climate simulations over the CORDEX-EA domain. *Atmos. Res.* **2019**, *224*, 81–98. https://doi.org/10.1016/j.atmosres.2019.03.020.
42. García-García, A.; Cuesta-Valero, F.J.; Beltrami, H.; González-Rouco, J.F.; García-Bustamante, E. WRF v.3.9 sensitivity to land surface model and horizontal resolution changes over North America. *Geosci. Model Dev.* **2022**, *15*, 413–428. https://doi.org/10.5194/gmd-15-413-2022.
43. Rauscher, S.A.; Coppola, E.; Piani, C.; Giorgi, F. Resolution effects on regional climate model simulations of seasonal precipitation over Europe. *Clim. Dyn.* **2010**, *35*, 685–711. https://doi.org/10.1007/s00382-009-0607-7.
44. Park, J.-H.; Oh, S.-G.; Suh, M.-S. Impacts of boundary conditions on the precipitation simulation of RegCM4 in the CORDEX East Asia domain. *J. Geophys. Res. Atmos.* **2013**, *118*, 1652–1667. https://doi.org/10.1002/jgrd.50159.
45. Miguez-Macho, G.; Stenchikov, G.L.; Robock, A. Spectral nudging to eliminate the effects of domain position and geometry in regional climate model simulations. *J. Geophys. Res. Atmos.* **2004**, *109*, D13104. https://doi.org/10.1029/2003JD004495.
46. Mooney, P.A.; Mulligan, F.J.; Fealy, R. Evaluation of the sensitivity of the weather research and forecasting model to parameterization schemes for regional climates of Europe over the period 1990-95. *J. Clim.* **2013**, *26*, 1002–1017. https://doi.org/10.1175/JCLI-D-11-00676.1.
47. Seo, G.-Y.; Choi, Y.-W.; Ahn, J.-B. Near Future Projection of Extreme Temperature over CORDEX-East Asia Phase 2 Region Using the WRF Model Based on RCP Scenarios. *Atmosphere* **2019**, *29*, 585–597. https://doi.org/10.14191/Atmos.2019.29.5.585. (In Korean)
48. Vannitsem, S.; Chomé, F. One-wa nested regional climate simulations and domain size. *J. Clim.* **2005**, *18*, 229–233. https://doi.org/10.1175/JCLI3252.1.

Disclaimer/Publisher's Note: The statements, opinions and data contained in all publications are solely those of the individual author(s) and contributor(s) and not of MDPI and/or the editor(s). MDPI and/or the editor(s) disclaim responsibility for any injury to people or property resulting from any ideas, methods, instructions or products referred to in the content.